Journal of Power Sources 252 (2014) 292–297

Contents lists available at ScienceDirect

Journal of Power Sources

journal homepage: www.elsevier.com/locate/jpowsour

Effect of Mg doping on the local structure of $LiMg_yCo_{1-y}O_2$ cathode material investigated by X-ray absorption spectroscopy

J.H. Cheng [a], C.J. Pan [a], C. Nithya [b], R. Thirunakaran [b], S. Gopukumar [b], C.H. Chen [a], J.F. Lee [c], J.M. Chen [c], A. Sivashanmugam [b,**], B.J. Hwang [a,c,*]

[a] Department of Chemical Engineering, National Taiwan University of Science and Technology, 43, Sec. 4, Keelung Rd., Taipei 106, Taiwan, ROC
[b] CSIR – Central Electrochemical Research Institute, Karaikudi 630 006, Tamil Nadu, India
[c] National Synchrotron Radiation Research Center (NSRRC), 101 Hsin-Ann Rd., Hsin Chu 30076, Taiwan, ROC

HIGHLIGHTS

- The oxidation state of cobalt is found to stay at 3^+ in Mg-doped $LiCoO_2$.
- Mg ions are found to sit on the transition metal layer.
- The oxygen is found to participate in the charge compensation.
- A charge compensation mechanism and oxygen vacancy is evidenced by XAS.

GRAPHICAL ABSTRACT

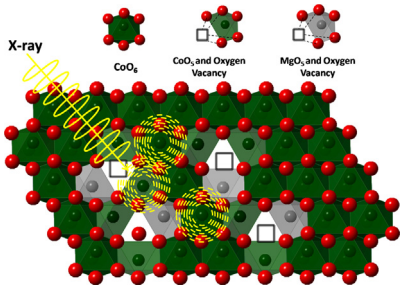

ARTICLE INFO

Article history:
Received 22 May 2013
Received in revised form
13 September 2013
Accepted 29 October 2013
Available online 15 November 2013

Keywords:
Cathode materials
$LiMg_yCo_{1-y}O_2$
Lithium-ion battery
X-ray absorption spectroscopy

ABSTRACT

A higher capacity and better cyclability are apparent when magnesium is introduced into the structure of $LiCoO_2$ ($y = 0.15$). XRD analysis of $LiMg_yCo_{1-y}O_2$ ($y = 0$, 0.1, 0.15), synthesized at 800 °C using a microwave assisted method, shows that the material is in the R-3m space group and to have a slightly expanded unit cell that increases with greater magnesium doping. Structural analysis by X-ray absorption spectroscopy (XAS) at the Co K-edge, L-edge and O K-edge shows that the magnesium is located in the transition metal layer rather than in the lithium layer and the charge balance results from the formation of oxygen vacancies rather than Co^{4+}, while cobalt remains in the 3+ oxidation state. Interestingly, oxygen is found to participate in the charge compensation. Both magnesium, in the transition metal layer, and the Co-defect structure are attributed to the contribution towards structural stabilization of $LiCoO_2$, thereby resulting in its enhanced electrochemical performance.

1. Introduction

Rechargeable lithium ion batteries have become the state-of-the-art power sources for portable electronics due to their high energy and power densities and good cyclability, which makes them prime candidates for electric vehicles (EVs) and electrochemical storage systems utilizing sustainable energy [1,2]. $LiCoO_2$ is commonly employed as a cathode material in Lithium-ion battery, due to its facile synthesis and high theoretical capacity (273 $mAhg^{-1}$) [3]. However, it also possesses some drawbacks in

* Corresponding author. Department of Chemical Engineering, National Taiwan University of Science and Technology, 43, Sec. 4, Keelung Rd., Taipei 106, Taiwan, ROC.
** Corresponding author.
E-mail addresses: sivashanmugam@ymail.com (A. Sivashanmugam), bjh@mail.ntust.edu.tw (B.J. Hwang).

0378-7753/$ – see front matter © 2013 Elsevier B.V. All rights reserved.
http://dx.doi.org/10.1016/j.jpowsour.2013.10.130

that it delivers only half of its theoretical capacity i.e., 140 $mAhg^{-1}$ during cycling, due to structural instability while charging up to 4.2 V, and capacity fading resulting from the dissolution of cobalt in the $LiCoO_2$ structure [4].

In order to stabilize structural stress, the literature suggest two important strategies: one is the doping of suitable metal ions at transition metal sites, such as Mg [5,6], Al [7] and Ti [8]; the other commonly suggested method is coating with inactive metal oxides e.g. MgO [9] and ZrO_2 [10], Al_2O_3 [11]. In practice the substitution of Mg for Co may be a better choice, due to its light weight and low cost.

In the literature, it has been reported that the electrochemical properties of $LiCoO_2$, such as capacity and stability, are significantly enhanced by the addition of Mg [5,6,12–14]. Additionally, the comparatively larger radii of Mg^{2+} compared to Co^{3+} enlarges the inter-layer space, i.e. the so-called "pillar effect" [6,15], which reduces the resistance to lithium-ion movement, while preventing structural collapse when a significant mass of lithium ions are extracted.

However, some issues remain with respect to the Mg doped system. One is the structure's charge balance; unlike Al^{3+} possessing the same charge as Co^{3+}, Mg^{2+} will cause the formation of Co^{4+} or an oxygen vacancy. Tukamoto *et al.*, have proposed that a charge balance results from the existence of small amount of Co^{4+} [5]; however, Delmas *et al.*, have suggested that charge compensation may be more complicated. Solid state NMR measurements, indicate that the oxygen vacancy and the intermediate Co^{3+} state balance the $LiMg_yCo_{1-y}O_2$ structure's charge; this finding is supported by a published first-principle computational study [16]. Similarly, the formation of oxygen vacancy also takes place in the lithium-overstoichiometric $LiCoO_2$ system [17]. Another unresolved issue is whether Mg is sited in the lithium plane or in the transition metal plane. Pouillerie *et al.*, reported that in the Mg doped $LiNiO_2$ system, some Mg will exist in the lithium layer due to the similar radii size of Mg^{2+} (0.72 Å) and Li^+ (0.76 Å) [15]. However, Dahn *et al.*, investigated the structure of $LiCoO_2$ with various Mg doping amounts using the Rietveld refinement and found that none of the Mg was in the lithium layer; however, the XRD provides the information more related to long-range structure. It is helpful to further discuss these issues by the tools which could provide some short-range information, such as X-ray Absorption Spectroscopy (XAS).

XAS is a powerful technique to probe both electronic structure and local structure of cathode materials. Information about the valence state of the investigated element and its electron configuration can be obtained from the X-ray absorption near-edge structure (XANES) region, whereas the extended X-ray absorption fine structure (EXAFS) region can provide the local structure of absorbing atom [18,19]. To investigate the above issues, both hard and soft XAS were used to provide detailed information related to the electronic states and local structure environments of Mg-doped $LiCoO_2$ synthesized by a microwave assisted method.

2. Experimental

Synthesis of $LiMg_yCo_{1-y}O_2$ ($y = 0.1, 0.15$) was carried out by mixing stoichiometric amounts of Li, Mg and Co acetates dissolved in a minimum volume of distilled water. The resulting concentrated metal ion solution was stirred continuously with slight warming (50 °C) and then transferred to a china dish and irradiated in a microwave oven (2450 MHz, 800 W) at 50% power for 20 min creating a red flame. After completion of the reaction, the product was dried in an air oven, calcined for 4 h and ground for 2 h to obtain a pure phase $LiMg_yCo_{1-y}O_2$. The synthesized product was characterized by synchrotron based XRD in beamline 01C2 at National Synchrotron Radiation Research Center (NSRRC), Hsinchu, Taiwan. The energy of the X-ray was set in 14 keV.

Hard XAS transmission mode spectroscopy was carried out in beam line 17C1 at NSRRC, using a Si (111) double crystal monochromator for energy selection with high-order harmonic contamination being rejected by mirrors. The intensities of the incident and transmitted beams were measured using gas ionization chambers. Energy calibration was performed in each scan by conducting simultaneous measurements on a reference Co foil.

Data from soft XAS measurements were acquired in total electron yield mode, for Co $L_{II,III}$-edge spectra, and in fluorescence mode for O K-edge spectra using an ultra high-vacuum (UHV) chamber with a base pressure of 1×10^{-10} Torr. The detection depths for the fluorescence mode and the total electron yield mode are around 3000 Å and smaller than 50 Å respectively, and the information obtained from these modes originates mainly from the surface and the bulk of the particle respectively [20].

Standard procedures were followed to analyze the EXAFS data. First, the raw absorption spectra in the pre-edge region were fitted to a straight line and the background above the edge was fitted with a cubic spline. The EXAFS function, χ, was obtained by subtracting the post edge background from the overall absorption and then normalized with respect to the edge jump step. The normalized $\chi(E)$ was transformed from energy space to k space, where k is the photoelectron wave vector. The $\chi(k)$ data were multiplied by k^3 to compensate for the damping of EXAFS oscillations in the high-k region. Subsequently, k^3-weighted $\chi(k)$ data in the k space ranging from 3.2 to 13.4 Å were Fourier transformed (FT) to r space in order to separate the EXAFS contributions from different coordination shells. A nonlinear least-squares algorithm was applied for curve fitting of EXAFS in r space between 1.04 and 4.0 Å. All the computer programs were implemented in the UWXAFS 3.0 software package with the backscattering amplitude and the phase shift for specific atom pair theoretically calculated by using FEFF7 code [21].

The cathode electrode was prepared by a slurry coating procedure from a mix comprising 80 wt% active materials, 10 wt% acetylene black and 10 wt% polyvinylidene fluoride (PVDF) binder in N–methylpyrrolidone (NMP) solvent. The slurry was coated over an aluminum foil and dried under ambient condition overnight and pressed under a 10 tons load. Discs (18 mm diameter) were cut and dried under vacuum at 120 °C for 12 h. Coin cells (2016 type) were assembled in an argon filled glove box, using the cathode disc in conjunction with lithium as the counter and reference electrode. A Celgard 2400 separator was used with $LiPF_6$ in 1:1 EC/DEC being used as the electrolyte. The charge–discharge measurements of the coin cells were carried out using a programmable battery tester at constant current rate of 0.1 C for 20 cycles in the potential range 3.0–4.2 V.

3. Results and discussion

3.1. X-ray diffraction

Fig. 1 shows the XRD patterns of $LiMg_yCo_{1-y}O_2$ ($y = 0.1, 0.15$) cathode materials calcined at 850 °C. All the peaks could be indexed to a α-$NaFeO_2$ type layered structure having the R-3m space group. The small peaks show in ~42 and ~63° are identified as slight existence of MgO impurity for the $LiMg_{0.1}Co_{0.9}O_2$ and $LiMg_{0.15}Co_{0.85}O_2$ samples. Since the amount of the MgO impurity is insignificant, it might not affect the electrochemical properties of the Mg-doped materials. The high intensity reflections of both patterns indicate the products' highly crystalline nature. Additionally, Mg doping leads to a slight expansion of inter atomic distance within a CoO_2 layer and an expansion in the interplanar distance between the CoO_2 layers. This trend has previously been noted

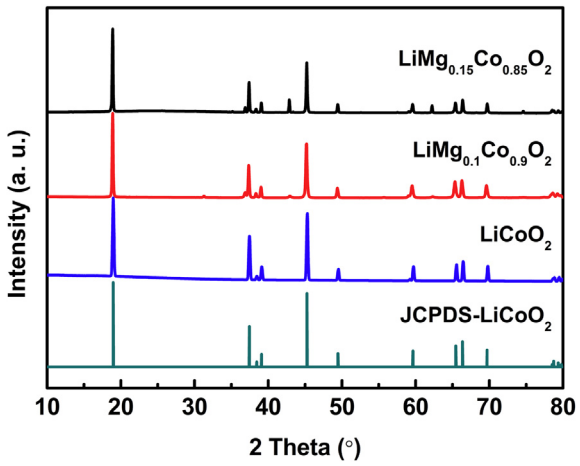

Fig. 1. XRD patterns of $LiCoO_2$ and $LiMg_yCo_{1-y}O_2$ (y = 0.1, 0.15) cathode material calcined at 850 °C.

[13,22]and has been ascribed to the larger ionic radii of Mg^{2+} (0.72Å) replacing Co^{3+} (0.57Å).

3.2. Electrochemical properties

Fig. 2 shows charge/discharge curves of $LiMg_yCo_{1-y}O_2$ calcined at 850 °C, cycled between potential limits of 3.0–4.2 V at 0.1C. The discharge capacities of Mg-doped $LiCoO_2$ materials are 162 and 145 $mAhg^{-1}$ (for x = 0.15 and 0.10 respectively), whereas $LiCoO_2$ cathode material synthesized by the same method delivers a discharge capacity of 125 $mAhg^{-1}$ at 0.1 C [12]. In the case of doped material, the Mg^{2+} occupancy in the inter-slab space with Co^{3+} facilitates the movement of Li^+ ions beyond 4.2 V Fig. 3 shows the cycle number versus the discharge capacity of $LiMg_yCo_{1-y}O_2$ cathodic material over 20 cycles at 0.1 C. The 20th cycle discharge capacities were 146 $mAhg^{-1}$ and 125 $mAhg^{-1}$ (for x = 0.15 and 0.1 respectively) representing only a 13% capacity fade, compared to $LiCoO_2$, where the 20th cycle discharge capacity was 80 $mAhg^{-1}$ with a capacity fade of 36%. The capacity fade of Mg-doped $LiCoO_2$ is relatively small compared to previous reports [23–26].

3.3. Co K-edge XAS

Fig. 4(a) shows the normalized Co K-edge XANES spectra for $LiCoO_2$ and $LiMg_yCo_{1-y}O_2$. The Co K-edge XANES spectrum arises

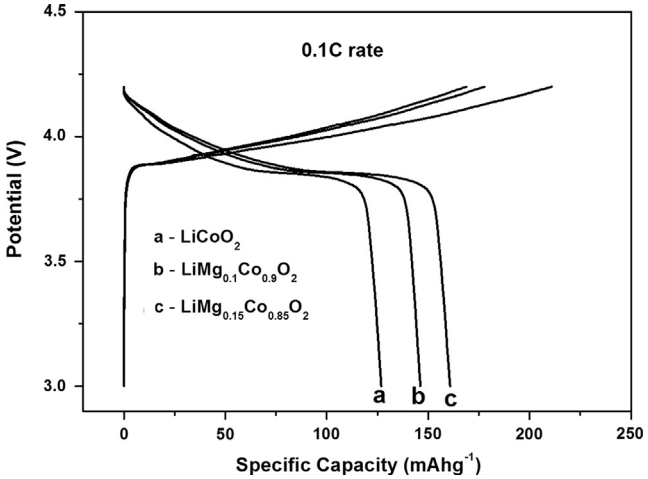

Fig. 2. Charge/discharge curves of $LiCoO_2$ and $LiMg_yCo_{1-y}O_2$ (y = 0.1, 0.15) cathode material calcined at 850 °C in the first cycle.

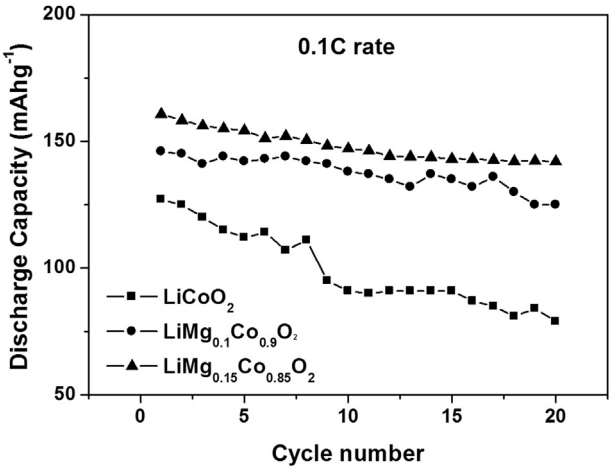

Fig. 3. Cycling performance of $LiCoO_2$ and $LiMg_yCo_{1-y}O_2$ (y = 0.1, 0.15) cathode material at 0.1C rate in the voltage range from 3.0 to 4.2 V.

from transitions of the 1s core electron of Co to excited vacant bound states in accordance with symmetry rules. The pre-edge absorption, peak-A, is assigned to a formal electric dipole-forbidden 1s to 3d transition, which gains peak intensity from pure electric quadrupole coupling and 3d–4p orbital mixing, due to the non-centro-symmetric environment of its slightly distorted CoO_6 octahedral site. The absorption peak-B can be assigned to a shakedown process involving the 1s to 4p transition followed by ligand-to-metal charge transfer (LMCT). The well resolved

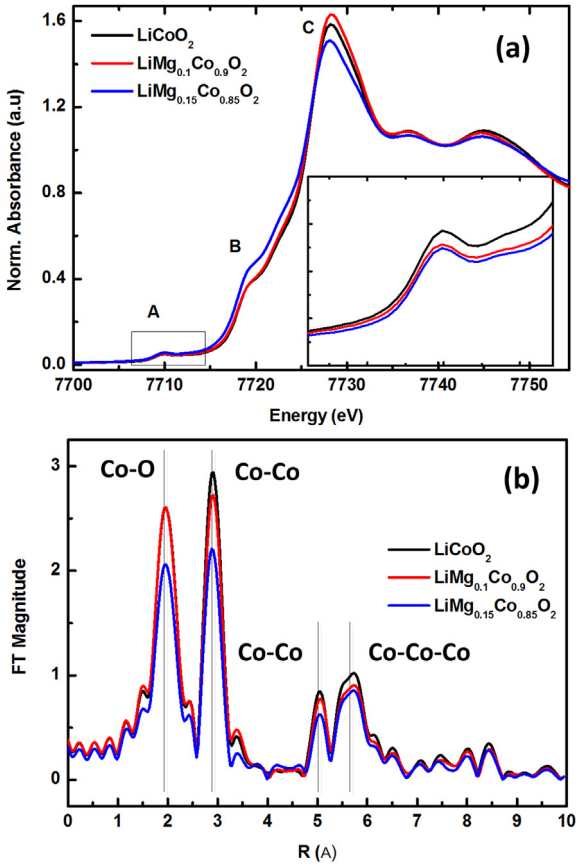

Fig. 4. (a) Normalized Co K-edge XANES and (b) Fourier transformed Co K-edge EXAFS spectra of $LiCoO_2$ and $LiMg_yCo_{1-y}O_2$ (y = 0.1, 0.15) cathode material.

absorption peak-C arises due to the dipole-allowed 1s to 4p transition. Peaks B and C correspond to two final states of $1s^1c3d^7L4p^1$, which result from shakedown processes by ligand-to-metal charge transfer, and a $1s^1c3d^64p^1$ state formed without a shakedown process, where c and L are a 1s core hole and a ligand hole. Peak B occurs as a shoulder in the lower-energy region, as the 1s core electron of the $3d^7L$ state, when compared to the $3d^6$ state, is less strongly bound. The edge excitation energy observed for both the pristine and Mg doped $LiCoO_2$ samples are the same. The more precise position could be found in the 1st derivatives of the edge, shown in Figure SI-1, which all the inflexion points do not move. This result indicates that doping with Mg does not cause a change in the oxidation state of the Co atom which is 3+ and implies an oxygen vacancy may be responsible for the charge balance rather than the existence of Co^{4+}. A closer examination of the pre-edge region (peaks A) could also confirm the peak position for all samples are the same, besides, after a background subtraction, shown in Figure SI-2, the intensity of the pre-edge peak increases as a doping amount increases. The intensity of the pre-edge represents the symmetric of the structure. A higher symmetry results in a smaller pre-edge peak. This result indicates with Mg doping, the crystal structure was slightly distorted either by Mg doping and/or by the formation of oxygen vacancies.

Fig. 4(b) shows the Fourier transformed (FT) spectra at the Co K-edges for $LiCoO_2$ and $LiMg_yCo_{1-y}O_2$ samples. Four scattering paths based on the crystal structure were observed. From XRD studies, layered $LiMg_yCo_{1-y}O_2$ exhibits an ideal symmetry, i.e. the hexagonal R-3m space group. In the crystallographic structure, the lithium atoms occupy a 3a site with the coordinates (0, 0, 0), the magnesium and cobalt atoms occupy a 3b site with the coordinates (0, 0, 0.5), and the oxygen atoms occupy a 6c site with the coordinates (0, 0, x). According to the symmetry of the hexagonal system, FT peaks result from single and multiple scattering paths.

The first peak at ca. 1.92 Å is due to the Co absorbing atom occupying the octahedral site surrounded by oxygen atoms in the first coordination shell (Co–O), while the second peak at ca. 2.82 Å is assigned to the contribution by Co and Mg atoms on the transition metal layer (Co–Co and Co–Mg). It is clear from Fig. 4 that there is no significant difference in the peak positions between the pristine and Mg-doped samples. The introduction of Mg into the $LiCoO_2$ structure does not significantly change the bonding length of Co–O and Co-metal. However, the peak intensities of $LiMg_yCo_{1-y}O_2$ are reduced with an increase in the Mg content. The reduction of the FT peak corresponding to the Co–Co interaction of $LiMg_yCo_{1-y}O_2$ may be attributed to the replacement of Co by Mg in the transition metal layer, as Mg atom has a lower scattering ability than Co. In the case of the addition of Mg in the structure of $LiCoO_2$, we also used CaRIne 3.1 to simulate the structure. And we selected $LiCo_{5/6}Mg_{1/6}O_2$ as for standard crystal to simulate the model of Co–O, Co–Co, and Co–Mg by FEFF7. Based on the standard crystal model, if we only focus local structure within 4 Å around the Co core atom, we could obtain 6 coordinate of the Co–O in the first shell. In the transition metal layer, there are 5 coordinate of the Co–Co and one coordinate of the Co–Mg in the standard crystal. The extracted structural parameters for the $LiMg_yCo_{1-y}O_2$ (y = 0, 0.1, 0.15) samples obtained by the curve fitting analysis are shown in Table 1. The three-shell theoretical fit (scatter line) matches closely with the back FT transformed experimental data (solid line) as shown in Fig. 5. Good fitting quality indicates that the Co–O, Co–Co, and Co–Mg bonds are reliable. The changes of coordination number, bond length, inner potential shift and Debye–Waller factor for the first shell Co–O and second Co–Co shell were extracted with different contents of Mg in $LiMg_yCo_{1-y}O_2$. With an increase in Mg doping, the coordination number of Co–O and Co–Co decreased gradually. The coordination numbers of Mg doping

Table 1
Fitting results of EXAFS data at Co K-edge for $LiMg_yCo_{1-y}O_2$ samples.

Samples	Shell	N	R_j (Å)	$\sigma^2 \times 10^{-3}$ (Å^2)	ΔE_0 (eV)	r-factor
$LiCoO_2$	Co–O	6.0 (±0.01)	1.912 (±0.003)	2.5 (±0.2)	11.2	0.001
	Co–Co	6.0 (±0.01)	2.822 (±0.003)	2.7 (±0.1)	8.7	
$LiMg_{0.1}Co_{0.9}O_2$	Co–O	5.60 (±0.08)	1.917 (±0.003)	4.8 (±0.5)	10.0	0.011
	Co–Co	4.80 (±0.09)	2.826 (±0.004)	3.3 (±0.6)	8.1	
	Co–Mg	0.70 (±0.11)	2.880 (±0.005)	8.8 (±0.3)	12.9	
$LiMg_{0.15}Co_{0.85}O_2$	Co–O	5.30 (±0.04)	1.919 (±0.004)	5.3 (±0.2)	7.9	0.021
	Co–Co	4.40 (±0.04)	2.824 (±0.003)	2.3 (±0.6)	10.0	
	Co–Mg	0.70 (±0.13)	2.883 (±0.007)	9.9 (±0.4)	14.4	

[Notation] N: coordination numbers; R_j (Å): interatomic distance; σ^2 (Å^2): Debye–Waller factor; ΔE_0 (eV): inner potential shift.

(y = 0.1 and 0.15) are 5.60 and 5.30 for Co–O, which provides evidence of the creation of oxygen vacancies, thereby confirming that only Co^{3+} exists in pristine Mg-doped $LiCoO_2$. Besides, the increase of the Debye–Waller factor from 2.5 to 5.3 for the $LiCoO_2$ and $LiMg_{0.15}Co_{0.85}O_2$ also implies the Mg doping caused some distortion of the local structure.

The FT peaks in the higher R region arise from single Co–Co and multiple Co–Co–Co scattering. From the $Li_xNi_{0.65}Co_{0.25}Mn_{0.1}O_2$ system reported by Hwang et al., [27] the FT peak at ca. 4.5 Å is dominated by the contribution of six M–M scattering interactions within the transition metal layer and six M–M scattering interactions from the two adjacent transition metal layers. The FT

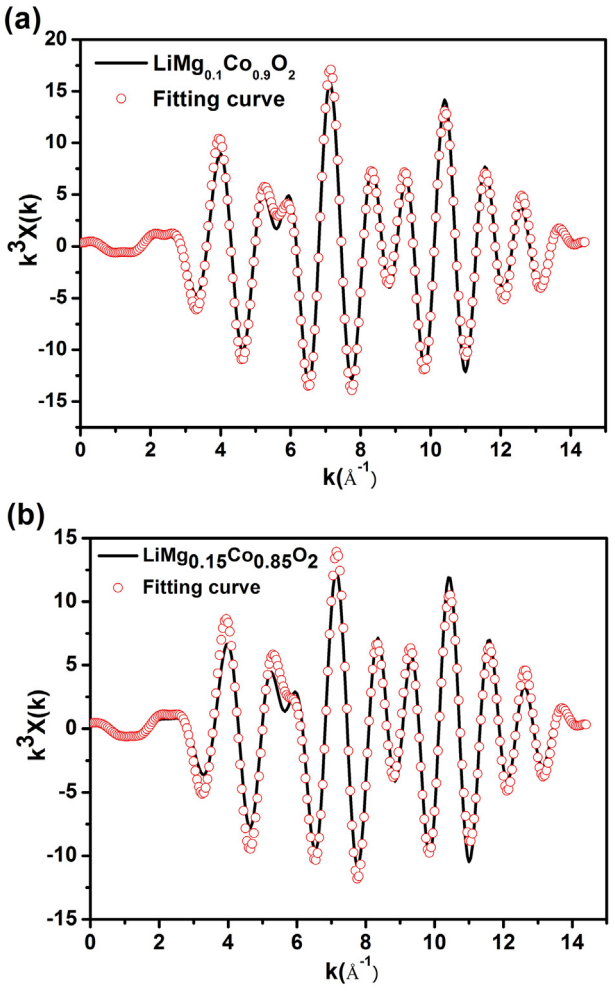

Fig. 5. The three-shell fits (scatter line) and back-transformed experimental EXAFS data (solid line) for (a) $LiMg_{0.1}Co_{0.9}O_2$ (b) $LiMg_{0.15}Co_{0.85}O_2$.

peak at ca. 5.2 Å is arises from the focusing effect of multiple M–M–M scattering interactions including 12 collinear atomic arrangements, where a second scattering atom lies collinearly between an emitting atom and a scattering atom. The reduction in the intensity of these two peaks can be attributed to the lower scattering ability of Mg atoms.

3.4. Co L-edge XAS

The electronic structures of Co-ion in the $LiMg_yCo_{1-y}O_2$ system were investigated qualitatively using soft XAS to investigate the peak shapes and chemical shifts which are very sensitive to the oxidation state, spin state, and bond covalence [28]. Fig. 6(a) shows the Co $L_{II,III}$-edge XAS spectra of the $LiMg_yCo_{1-y}O_2$ system with respect to the y value. The L_{III} and L_{II} edges corresponded to transitions from the Co $2p_{3/2}$ and $2p_{1/2}$ core electrons respectively, split by spin-orbital interactions of the Co 2p core level to an unoccupied 3d level hybridized with an oxygen 2p orbital. When compared to $LiCoO_2$, the main peak of Co L_{III} and the L_{II} edges for the Mg-doped samples show no shifts and remain located at ca. 782.4 and 796.8 eV, respectively, confirming again that the oxidation state of Co in the Mg-doped $LiCoO_2$ is 3+. The peak position could be seen clearer when laying over, shown in Figure SI-3. Additional peaks before the main peak are due to the slight distortion of CoO_6 symmetry [29], which may be caused by the formation of oxygen vacancies.

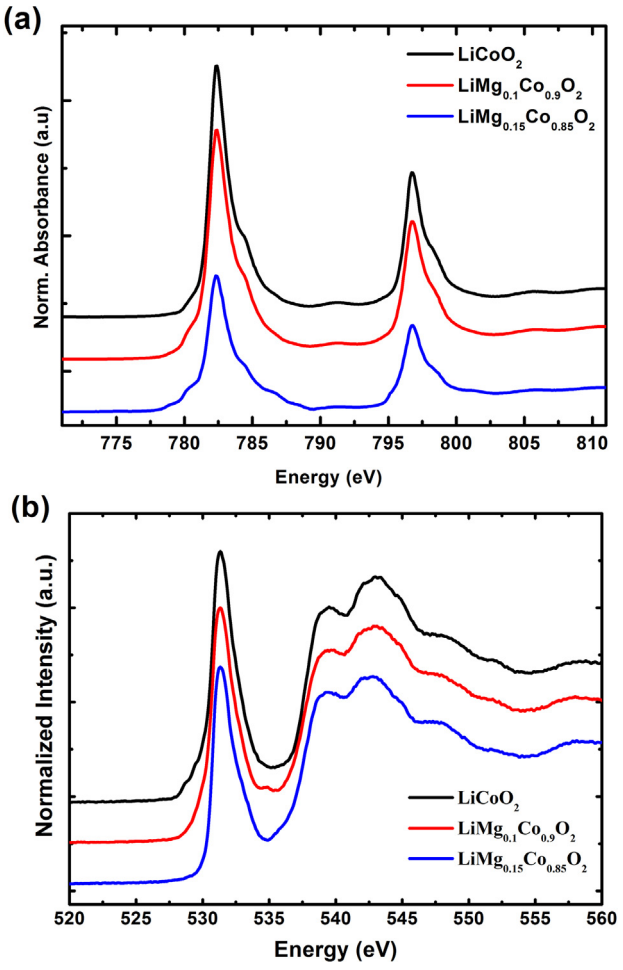

Fig. 6. (a) Co $L_{II,III}$-edge (b) O K-edge spectra of $LiCoO_2$ and $LiMg_yCo_{1-y}O_2$ ($y = 0.1, 0.15$) cathode material.

3.5. O K-edge XAS

The pre-edge peak positions and intensity of oxygen K-edge XAS spectra provide important structural information about the bonding between transition metal atoms and oxygen ligands. The O K-edge XAS of the Mg-doped $LiCoO_2$ system is shown in Fig. 6(b). Pre-edge peaks below ~535 eV all correspond to the transition of oxygen 1s electron to the hybridized state of the transition metal 3d and oxygen 2p orbitals [30], whereas the broad peaks in the higher energy region above ~545 eV correspond to the transition to hybridized states of the 2p oxygen and 4sp transition metal orbitals [31].

Two major changes in the spectral features, caused by Mg doping, were observed in the pre-edge region: a shift to higher threshold energy in the pre-edge peak position and a decrease in the integrated peak intensity. The peak intensity decreases with an increase in amount of Mg doping. The variation of the peak intensity with Mg doping can give important structural information about the whole state distribution. As the density of the empty bound state at the molecular level is related to the hybridization of Co 3d–O 2p orbitals, the decrease in the peak intensity is due to a decrease in bond covalency. The variation of bond covalency is probably due to molecular re-hybridization between the Co 3d–O 2p orbitals, resulting from local structural distortion around the Co ion, due to the presence of oxygen vacancies. It has previously been reported that octahedral distortion can lead to changes in bond covalency [30,32].

The chemical shift in the ligand 1s core threshold energy is related to the effective charge on the ligand. Higher excitation energy is required for oxygen, having a higher degree of oxidation, in order to promote the oxygen 1s electron. Therefore, the threshold energy shift (with Mg-doping) to a higher energy level can be attributed to oxygen sites being in higher oxidation states indicating that charge compensation for Mg-doped $LiCoO_2$ materials can also be partially achieved at the oxygen sites. The participation of oxygen in compensating charge variations in cathode materials has also been noted theoretically by Ceder *et al.* [33], and experimentally by Yoon *et al.* [30]

The Co K-edge and L-edge XAS spectra show the oxidation state of Co to be 3+ for all Mg-doped samples. The formation of oxygen vacancies compensates the charge balance resulting from Mg doping. Partial charge compensation also occurs at oxygen sites, where some electron density is resulting in the nucleus strongly binding the residual electrons, thereby requiring higher X-ray energies to excite the 1s electron from the bound state to the empty unoccupied orbital.

4. Conclusion

Pure phase $LiCoO_2$ and $LiMg_yCo_{1-y}O_2$ ($y = 0.1, 0.15$) powders were successfully synthesized using a microwave based synthetic procedure. The best electrochemical performance was found with $LiMg_{0.15}Co_{0.85}O_2$. The Co K-edge and L-edge XAS spectra showed Co to be in the 3+ oxidation state for all the Mg-doped $LiCoO_2$ samples. The formation of oxygen vacancies is ascribed to charge balance compensation. For the O K-edge XAS, the threshold energy shifting to a higher energy on Mg doping can be assigned to the oxygen sites being in higher oxidation states, this also indicates that charge compensation for Mg-doped $LiCoO_2$ materials can also be partially achieved at the oxygen sites. From the EXAFS results, it is found that Mg is mainly confined to the transition metal layer where it contributes to oxygen vacancy formation. The Mg in the transition metal layer together with a Co-defect structure is thought to jointly contribute to the enhanced performance of Mg-doped $LiCoO_2$.

Acknowledgment

The authors are gratefully acknowledge support given under the Indo-Taiwan Collaborative Project (NSC-98-2923-M-011-001-MY, NSC-102-3113-E-011-002, MOEA-102-EC-17-A-08-S1-183) by the Department of Science and Technology, India and the National Science Council, Taiwan.

Appendix A. Supplementary data

Supplementary data related to this article can be found at http://dx.doi.org/10.1016/j.jpowsour.2013.10.130.

References

[1] B. Scrosati, J. Garche, J. Power Sources 195 (2010) 2419–2430.
[2] O.K. Park, Y. Cho, S. Lee, H.-C. Yoo, H.-K. Song, J. Cho, Energy Environ. Sci. 4 (2011) 1621.
[3] K. Mizushima, P.C. Jones, P.J. Wiseman, J.B. Goodenough, Mater. Res. Bull. 15 (1980) 783–789.
[4] G.G. Amatucci, J.M. Tarascon, L.C. Klein, Solid State Ionics 83 (1996) 167–173.
[5] H. Tukamoto, A.R. West, J. Electrochem. Soc. 144 (1997) 3164–3168.
[6] H.-S. Kim, T.-K. Ko, B.-K. Na, W.I. Cho, B.W. Chao, J. Power Sources 138 (2004) 232–239.
[7] S.-T. Myung, N. Kumagai, S. Komaba, H.-T. Chung, Solid State Ionics 139 (2001) 47–56.
[8] S. Gopukumar, Y. Jeong, K.B. Kim, Solid State Ionics 159 (2003) 223–232.
[9] M. Mladenov, R. Stoyanova, E. Zhecheva, S. Vassilev, Electrochem. Commun. 3 (2001) 410–416.
[10] S.-K. Hu, G.-H. Cheng, M.-Y. Cheng, B.-J. Hwang, R. Santhanam, J. Power Sources 188 (2009) 564–569.
[11] J. Cho, Y.J. Kim, B. Park, Chem. Mater. 12 (2000) 3788–3791.
[12] C.N. Zaheena, C. Nithya, R. Thirunakaran, A. Sivashanmugam, S. Gopukumar, Electrochim. Acta 54 (2009) 2877–2882.
[13] W. Luo, X. Li, J.R. Dahn, J. Electrochem. Soc. 157 (2010) A782–A790.
[14] H.-J. Kim, Y.U. Jeong, J.-H. Lee, J.-J. Kim, J. Power Sourc. 159 (2006) 233–236.
[15] C. Pouillerie, L. Croguennec, P. Biensan, P. Willmann, C. Delmas, J. Electrochem. Soc. 147 (2000) 2061–2069.
[16] X.G. Xu, C. Li, J.X. Li, U. Kolb, F. Wu, G. Chen, J. Phys. Chem. B 107 (2003) 11648–11651.
[17] S. Levasseur, M. Ménétrier, Y. Shao-Horn, L. Gautier, A. Audemer, G. Demazeau, A. Largeteau, C. Delmas, Chem. Mater. 15 (2002) 348–354.
[18] W.-S. Yoon, K.-K. Lee, K.-B. Kim, J. Electrochem. Soc. 149 (2002) A146–A151.
[19] H. Ohzono, M. Kouno, H. Miyake, H. Ohyama, Anal. Sci. 17 (2001) 3.
[20] J. McBreen, J. Solid State Electrochem. 13 (2008) 1051–1061.
[21] B. Ravel, M. Newville, J. Synchrotron Radiat. 12 (2005) 537–541.
[22] C. Julien, Solid State Ionics 157 (2003) 57–71.
[23] S. Rodrigues, N. Munichandraiah, A.K. Shukla, J. Power Sources 102 (2001) 322–325.
[24] C. Julien, M.A. Camacho-Lopez, T. Mohan, S. Chitra, P. Kalyani, S. Gopukumar, Solid State Ionics 135 (2000) 241–248.
[25] G.T.-K. Fey, P. Muralidharan, C.-Z. Lu, Y.-D. Cho, Electrochim. Acta 51 (2006) 4850–4858.
[26] H.-W. Ha, N.J. Yun, M.H. Kim, M.H. Woo, K. Kim, Electrochim. Acta 51 (2006) 3297–3302.
[27] Y.W. Tsai, J.F. Lee, D.G. Liu, B.J. Hwang, J. Mater. Chem. 14 (2004) 958.
[28] W. Yang, X. Liu, R. Qiao, P. Olalde-Velasco, J.D. Spear, L. Roseguo, J.X. Pepper, Y.-d. Chuang, J.D. Denlinger, Z. Hussain, J. Electron Spectrosc. Relat. Phenom. (2013) in press, http://dx.doi.org/10.1016/j.elspec.2013.03.008.
[29] B. Hedman, K.O. Hodgson, E.I. Solomon, J. Am. Chem. Soc. 112 (1990) 1643–1645.
[30] W.-S. Yoon, M. Balasubramanian, K.Y. Chung, X.-Q. Yang, J. McBreen, C.P. Grey, D.A. Fischer, J. Am. Chem. Soc. 127 (2005) 17479–17487.
[31] W.-S. Yoon, K.-B. Kim, M.-G. Kim, M.-K. Lee, H.-J. Shin, J.-M. Lee, J. Electrochem. Soc. 149 (2002) A1305–A1309.
[32] C.-H. Chen, B.-J. Hwang, C.-Y. Chen, S.-K. Hu, J.-M. Chen, H.-S. Sheu, J.-F. Lee, J. Power Sources 174 (2007) 938–943.
[33] G. Ceder, Y.M. Chiang, D.R. Sadoway, M.K. Aydinol, Y.I. Jang, B. Huang, Nature 392 (1998) 694–696.